Structures, Li⁺ mobilities, and interfacial properties of solid electrolytes Li₃PS₄ and Li₃PO₄ from first principles

N. D. Lepley, N. A. W. Holzwarth,[*] and Yaojun A. Du[†]

Department of Physics, Wake Forest University, Winston-Salem, North Carolina 27109, USA

This work reports a computer modeling comparison of two solid electrolyte materials, Li₃PO₄ and Li₃PS₄, in terms of the bulk structures, Li ion mobilities, and their interface properties with vacuum and with Li metal. The simulations show that for some forms of Li₃PS₄, Li ions can move from a host lattice site to an interstitial site with negligible net energy change. This favorable process for the formation of vacancy-interstitial pairs is undoubtedly important for the structural and ion migration properties of β-Li₃PS₄. Our model results for the idealized interfaces between the electrolytes and Li metal show that Li₃PO₄ /Li interfaces are stable, while Li₃PS₄ /Li interfaces are not. We find that a Li₃PS₄ surface in the presence of a small amount of Li relaxes to a complicated structure involving broken P-S bonds. On the other hand, the computer models show that a very thin film of Li₂S on the Li₃PS₄ surface can provide a protective buffer layer to stabilize the interface between the Li₃PS₄ electrolytes and the Li metal anode.

I. INTRODUCTION

Lithium thiophosphate, Li₃PS₄, has been shown[1–4] to be a very promising electrolyte material. It has interesting structural properties and ionic conductivities compared with its lithium phosphate analog[5,6] Li₃PO₄ which was the subject of previous investigations.[7,8] The focus of the present work is to study, via computer modeling, the detailed relationship between Li₃PS₄ and Li₃PO₄, including the bulk structures, the Li ion vacancy and interstitial defect structures, the Li ion mobilities, and the properties of the interfaces with vacuum and with Li metal. The results of this study together with experimental results reported in the literature are analyzed from the viewpoint of solid-state battery technology.

Promising advances in all-solid-state lithium battery technology provide the general motivation for this study. As pointed out in several recent reviews,[9–11] an all-solid-state battery design offers several advantages over current battery technologies including stability, efficiency, and safety. The prospects for battery designs with solid electrolytes were recently encouraged by the discovery[12] of the crystalline electrolyte Li₁₀GeP₂S₁₂ with a room-temperature ionic conductivity comparable to that of liquid electrolytes. In addition, the development[1] of a nanoporous form of Li₃PS₄ with improved ionic conductivity compared to previous preparations[2,3] also shows significant technological promise.

The paper is organized as follows. Section II presents the calculational methods used in this work. Results are presented in Sec. III. Section III A presents a comparison of the bulk structures of the two materials and their heats of formation. The two materials have very similar but not identical crystal structures. One of the phases of Li₃PS₄ is experimentally known to have disorder on some of its Li sites. We examine ordered idealizations of these structures. The calculated heats of formation provide information about the stabilities of the various phases of the materials and also crudely approximate reaction and decomposition energetics. Section III B presents results on Li ion vacancies and interstitials and their migration and formation properties within supercells of the bulk materials. The calculated activation energies for Li ion conductivities

are compared with corresponding results from experimental measurements. Interfaces of the electrolyte with vacuum and with Li metal are discussed in Sec. III C. Section IV presents a discussion and conclusions of the work.

II. CALCULATIONAL METHODS

The calculational methods in this work are based on density functional theory,[13,14] using the projector augmented wave (PAW)[15] formalism. The PAW basis and projector functions were generated by the ATOMPAW[16] code and used in both the ABINIT[17] and QUANTUM ESPRESSO[18] packages. The exchange-correlation functional was the local-density approximation (LDA).[19] The choice of the LDA functional was made on the basis of previous investigations[7] of Li₃PO₄. In that work, we showed that while the LDA results systematically underestimated the size of the lattice parameters, the LDA results for high-frequency phonon frequencies were in much better agreement with experiment than those obtained using the generalized gradient approximation[20] (GGA) functional. In the same work, we showed that the computed fractional atomic coordinates are very close to experimental results and that the energetics associated with Li⁺ migration are computed to be very similar in both LDA and GGA approximations.

For analyzing formation energies and other perfect crystal properties, calculations were performed with plane-wave expansions of the wave function including $|\mathbf{k} + \mathbf{G}|^2 \leqslant 64$ bohrs⁻² and with a Brillouin-zone sampling grid density of at least 10^{-3} bohrs⁻³/**k** point. In fact, structural parameters and relative energies were well converged with a smaller number of plane waves ($|\mathbf{k} + \mathbf{G}|^2 \leqslant 49$ bohrs⁻²) and a sparser Brillouin-zone sampling (0.02 bohrs⁻³/**k** point), so that simulations requiring larger supercells could be well approximated using these less stringent convergence parameters. Li vacancies and interstitials were modeled in supercells containing 16 formula units of Li₃PO₄ or Li₃PS₄. These supercells were used to estimate migration energies (E_m) for Li ion migration with the "nudged elastic band" (NEB) method,[21–23] as programed in the QUANTUM ESPRESSO package. The "formation energies" E_f

for producing vacancy-interstitial defects were calculated for the same supercells. Surface properties were modeled using a slab geometry within supercells containing an additional 10 bohrs representing the vacuum region. Properties of the interface with Li were modeled using a periodic array of electrolyte and metallic slabs. The volume available for the lithium slabs was determined by constrained optimization.

The partial densities of states $N^a(E)$ were calculated as programed in the ABINIT[17] package,[24] based on an expression of the form

$$N^a(E) = \sum_{n\mathbf{k}} W_{n\mathbf{k}} Q_{n\mathbf{k}}^a \delta(E - E_{n\mathbf{k}}). \qquad (1)$$

In this expression a denotes an atomic site, $W_{n\mathbf{k}}$ denotes the Brillouin-zone sampling and degeneracy weight factor for band index n and wave vector $\mathbf{k}$, and $E_{n\mathbf{k}}$ denotes the corresponding band energy. For each eigenstate $n\mathbf{k}$ and atomic site a, the local density of states factor $Q_{n\mathbf{k}}^a$ is given by the charge within the augmentation sphere of radius r_c^a which can be well approximated by

$$Q_{n\mathbf{k}}^a \approx \sum_{ij} \langle \widetilde{\Psi}_{n\mathbf{k}} | p_{n_i l_i m_i}^a \rangle \langle p_{n_j l_j m_i}^a | \widetilde{\Psi}_{n\mathbf{k}} \rangle q_{n_i l_i; n_j l_i}^a \delta_{l_i l_j}, \qquad (2)$$

in terms of the radial integrals

$$q_{n_i l_i; n_j l_i}^a \equiv \int_0^{r_c^a} dr\ \varphi_{n_i l_i}^a(r) \varphi_{n_j l_i}^a(r). \qquad (3)$$

In these expressions, $|\widetilde{\Psi}_{n\mathbf{k}}\rangle$ represents the pseudo-wave function, $|\widetilde{p}_{n_i l_i m_i}^a\rangle$ represents the PAW atomic projector function which is localized within the augmentation sphere about the atomic site a, and $n_i l_i m_i$ denotes radial and spherical harmonic indices of the projector function.[15,25] The function $\varphi_{n_i l_i}^a(r)$ represents an all-electron radial basis function. The augmentation radii used in this work are $r_c^{Li} = 1.6$, $r_c^O = 1.2$, $r_c^P = 1.7$, and $r_c^S = 1.7$ in bohr units. Visualizations were constructed using the XCRYSDEN[26,27] and VESTA[28] software packages.

III. RESULTS

A. Properties of bulk materials

1. Crystal structures

The crystal structures of Li_3PO_4 and Li_3PS_4 are very similar but not identical. For both compounds, the most stable structures are characterized by two different space groups which are designated in the International Table of Crystallography[29] by a high-symmetry $Pnma$ (no. 62) structure and a lower-symmetry $Pmn2_1$ (no. 31) structure. In this paper we will follow the naming conventions of the previous literature. For lithium phosphate, β-Li_3PO_4 refers to the $Pmn2_1$ structure and γ-Li_3PO_4 refers to the $Pnma$ structure. By contrast for lithium thiophosphate, γ-Li_3PS_4 refers to the $Pmn2_1$ structure and β-Li_3PS_4 refers to the $Pnma$ structure.[30]

The lowest energy structure for both materials is characterized by the $Pmn2_1$ space group.[2,6] For both Li_3PO_4 and Li_3PS_4, this structure is well defined in the sense that the Wyckoff sites are fully occupied. While the lattice constants of Li_3PO_4 are approximately 80% of those of Li_3PS_4, the fractional coordinates of the two materials are nearly identical
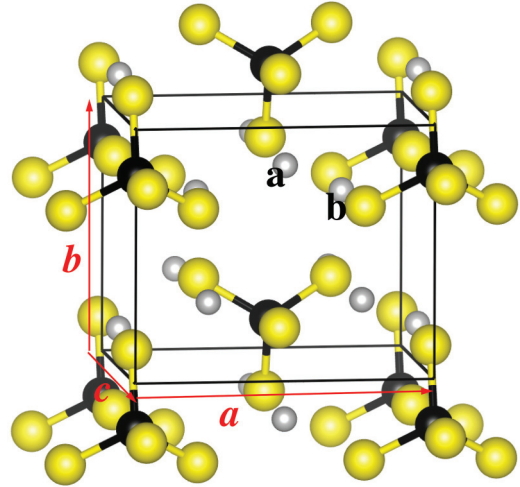

FIG. 1. (Color online) Ball and stick diagram of the unit cell of the $Pmn2_1$ structure of γ-Li_3PS_4. The Li, P, and S sites are depicted with gray, black, and yellow balls, respectively. The roman "a" and "b" indicate examples of Li sites with those Wyckoff labels.

as reported in previous work.[31] A structural diagram of γ-Li_3PS_4 is shown in Fig. 1. Table I lists the optimized lattice constants calculated for γ-Li_3PS_4 in comparison with the experimental results of Homma *et al.*[2] who identified this phase at room temperature. The corresponding comparison for β-Li_3PO_4 was presented in earlier work.[7] As expected for calculations using the LDA exchange-correlation functional, the lattice constants are systematically underestimated, but the fractional coordinates are well modeled.

The higher energy $Pnma$ structures for both Li_3PO_4 and Li_3PS_4 have also been well studied experimentally. For Li_3PO_4, the phase transition from the $Pmn2_1$ to the $Pnma$ structure has been observed at 500 °C,[6] however the high-temperature phase material has also been observed and studied at lower temperatures. The phase transformation of β-Li_3PS_4 is more complicated. Single-crystal β-Li_3PS_4 was prepared by Mercier *et al.*[4] by slow cooling from 500 °C and analyzed to have the $Pnma$ structure in 1982. On the basis of differential thermal analysis, a phase transformation was reported at 200 °C in 1984,[3] however, it was not until 2011 that Homma *et al.*[2] determined the structures of both phases from powdered samples. There is good agreement between the structural results of Homma *et al.*[2] measured at 364 °C and Mercier *et al.*[4] measured at room temperature for the $Pnma$ phase of Li_3PS_4. The differential thermal analysis by Homma *et al.*[2] finds the phase transformation to occur reversibly between 270 and 364 °C. The early results of Mercier *et al.*[4] and the more recent results of Liu *et al.*[1] show that it is possible to prepare β-Li_3PS_4 at room temperature.

The detailed structures of the $Pnma$ materials are more complicated than those of the $Pmn2_1$ materials. In γ-Li_3PO_4, the structure is described by full occupancy of the crystallographic sites,[32] as shown in Fig. 2. A comparison of Figs. 1 and 2 shows that a crude approximation to the $Pnma$ structure can be derived from the $Pnm2_1$ structure by switching the **a** and **b** axes and then doubling the unit cell along the **a** axis. Additional differences are due to the orientation of the phosphate or thiophosphate tetrahedra along the **c** axis. For

TABLE I. Lattice parameters and fractional atomic positions for $Pmn2_1$ crystals of γ-Li$_3$PS$_4$, comparing calculated values ("Calc.") with the experimental results measured at room temperature as reported in Ref. 2 ("Expt."). The atomic sites are designated with their multiplicity in the unit cell and their standard Wyckoff label as defined in Ref. 29.

		Calc.	Expt.
Lattice parameters		Å	Å
	a	7.55	7.71
	b	6.45	6.54
	c	6.05	6.14
Atom	Site	(x,y,z)	(x,y,z)
Li	4b	(0.243, 0.317, 0.000)	(0.250, 0.331, 0.018)
Li	2a	(0.000, 0.150, 0.488)	(0.000, 0.145, 0.486)
P	2a	(0.000, 0.819, 0.999)	(0.000, 0.822, 0.994)
S	4b	(0.221, 0.670, 0.888)	(0.219, 0.672, 0.886)
S	2a	(0.000, 0.118, 0.886)	(0.000, 0.108, 0.888)
S	2a	(0.000, 0.811, 0.337)	(0.000, 0.805, 0.323)

the $Pnma$ Li$_3$PS$_4$ materials, further complication comes from the fact that in β-Li$_3$PS$_4$, some of the Li sites are partially occupied[2,4]—namely the site labeled "b" in the Wyckoff notation is found to have an occupancy of 70% while the site labeled "c" is found to have an occupancy of 30%. In order to perform simulations on idealized perfect crystals, we considered three variations. The β-Li$_3$PS$_4$-b variation has 100% occupancy of the b site. The β-Li$_3$PS$_4$-c variation has 100% occupancy of the c site. These structures are visualized in Fig. 3. We also studied the β-Li$_3$PS$_4$-c' structure which was computationally constructed by optimizing Li$_3$PS$_4$ starting with the fractional coordinates of γ-Li$_3$PO$_4$. The constructed β-Li$_3$PS$_4$-c' structure has 100% occupancy of a c site, but the optimized fractional coordinates are much closer to those of γ-Li$_3$PO$_4$ (shown in Fig. 2) than to the coordinates of

the other Li$_3$PS$_4$ structures. The three idealized structures for β-Li$_3$PS$_4$ are compared with each other and with experiment in Table II. The corresponding results for Li$_3$PO$_4$ have been presented in previous work.[7] Interestingly, while the linear dimensions of the phosphate materials are approximately 80% of those of the thiophosphates, the fractional coordinates of the corresponding structure (β-Li$_3$PS$_4$-c') are generally the same within ± 0.03.

2. Heats of formation

An important result from computer optimization of the various crystal structures is an assessment of the relative stabilities of the idealized structures of the lithium phosphates and thiophosphates considered in this study. It is convenient to use
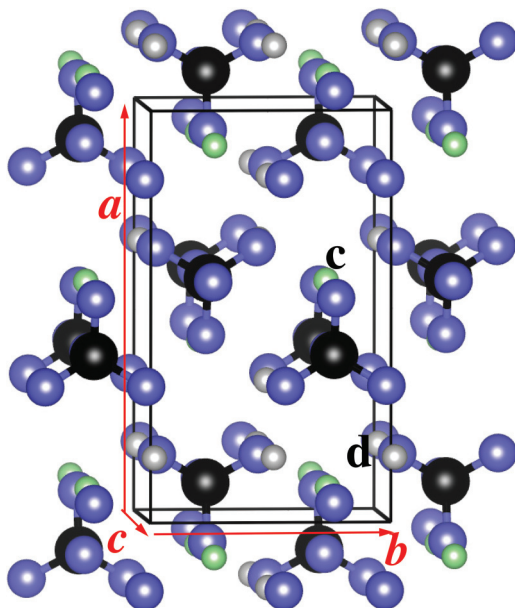

FIG. 2. (Color online) Ball and stick diagram of the unit cell of $Pnma$ structure of γ-Li$_3$PO$_4$. The P and O sites are depicted with black and blue balls, respectively. The Li sites are shown with gray and green balls for the Wyckoff "d" and "c" sites, respectively.
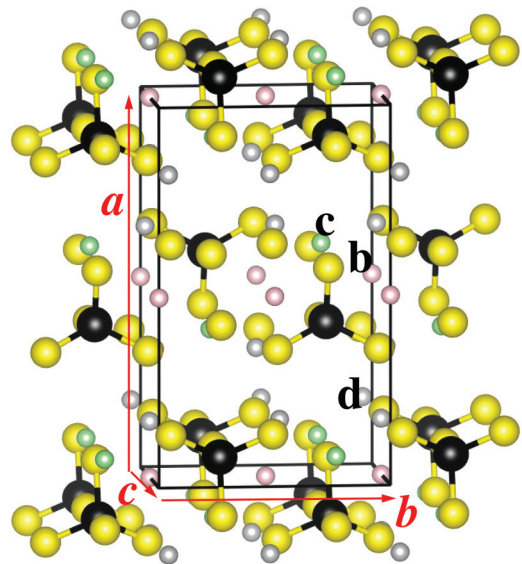

FIG. 3. (Color online) Ball and stick diagram of the unit cell of $Pnma$ structures of Li$_3$PS$_4$. The P and S sites are depicted with black and yellow balls, respectively. The Li sites are shown with gray balls for the Wyckoff d sites. The pink balls correspond to the b sites occupied in the β-Li$_3$PS$_4$-b structure while the green balls correspond to the c sites occupied in the β-Li$_3$PS$_4$-c structure.

TABLE II. Optimized lattice parameters and fractional atomic positions for three idealized structures of β-Li$_3$PS$_4$ compared with the experimental structure reported in Ref. 2 at 364 °C. In the experimental structure, the Li $4b$ sites have an occupation factor of 70%, while the Li $4c$ sites have an occupation factor of 30%. In the idealized structures, the occupation factors are 100% for all sites. The notation is the same as that in Table I.

		β-Li$_3$PS$_4$-b	β-Li$_3$PS$_4$-c	β-Li$_3$PS$_4$-c'	Expt.
Lattice parameters		Å	Å	Å	Å
	a	12.86	12.45	13.11	12.82
	b	7.81	7.76	7.79	8.22
	c	5.94	6.21	5.91	6.12
Atom	Site	(x,y,z)	(x,y,z)	(x,y,z)	(x,y,z)
Li	$8d$	(0.331, 0.031, 0.371)	(0.346, 0.001, 0.159)	(0.341, 0.006, 0.297)	(0.356, 0.013, 0.439)
Li	$4b$	(0.000, 0.000, 0.500)	(N/A)	(N/A)	(0.000, 0.000, 0.500)
Li	$4c$	N/A	(0.910, 0.250, 0.844)	(0.927, 0.250, 0.776)	(0.999, 0.250, 0.889)
P	$4c$	(0.088, 0.250, 0.143)	(0.093, 0.250, 0.161)	(0.093, 0.250, 0.312)	(0.087, 0.250, 0.171)
S	$8d$	(0.153, 0.030, 0.263)	(0.165, 0.034, 0.279)	(0.166, 0.034, 0.202)	(0.155, 0.046, 0.285)
S	$4c$	(0.939, 0.250, 0.278)	(0.933, 0.250, 0.230)	(0.946, 0.250, 0.206)	(0.935, 0.250, 0.257)
S	$4c$	(0.096, 0.250, 0.802)	(0.103, 0.250, 0.832)	(0.098, 0.250, 0.658)	(0.107, 0.250, 0.837)

the optimized energies found in these calculations to estimate the heat of formation for each material using the methods described in our earlier work.[31,33] The heat of formation of a material is determined relative to its decomposition into elemental materials in their standard states as defined in the CRC Handbook,[34] and the results are presented in Table III.

The energies of the lithium phosphate and thiophosphate materials reported in Table III show that the $Pmn2_1$ phases

TABLE III. Heats of formation per formula unit calculated for the listed reference and lithium phosphate and thiophosphate materials. The structure is described in terms of the space group using the notation of Ref. 29. When available, experimental values of ΔH from Ref. 34 and/or Ref. 35 are also listed.

Material	Structure	ΔH_{cal} (eV)	ΔH_{exp} (eV)
β-Li$_3$PO$_4$	$Pmn2_1$ (no. 31)	−21.23	
γ-Li$_3$PO$_4$	$Pnma$ (no. 62)	−21.20	−21.72
γ-Li$_3$PS$_4$	$Pmn2_1$ (no. 31)	−8.37	
β-Li$_3$PS$_4$-b	$Pnma$ (no. 62)	−8.28	
β-Li$_3$PS$_4$-c	$Pnma$ (no. 62)	−8.25	
β-Li$_3$PS$_4$-c'	$Pnma$ (no. 62)	−8.18	
Li$_2$O	$Fm\bar{3}m$ (no. 225)	−6.10	−6.20
Li$_2$O$_2$	$P6_3/mmc$ (no. 194)	−6.35	−6.57
Li$_2$S	$Fm\bar{3}m$ (no. 225)	−4.30	−4.57
Li$_2$S$_2$	$P6_3/mmc$ (no. 194)	−4.09	
α-Li$_3$N	$P6/mmm$ (no. 191)	−1.60	−1.71
Li$_3$P	$P6_3/mmc$ (no. 194)	−3.47	
LiNO$_3$	$R\bar{3}c$ (no. 167)	−5.37	−5.01
LiPN$_2$	$I\bar{4}2d$ (no. 122)	−3.65	
LiPO$_3$	$P2/c$ (no. 13)	−12.75	
Li$_2$SO$_4$	$P2_1/c$ (no. 14)	−14.63	−14.89
N$_2$O$_5$	$P6_3/mmc$ (no. 194)	−0.94	−0.45
P$_3$N$_5$	$C2/c$ (no. 15)	−3.02	−3.32
h-P$_2$O$_5$	$R3c$ (no. 161)	−15.45	−15.53
o-P$_2$O$_5$	$Fddd2$ (no. 43)	−15.78	
P$_4$S$_3$	$Pnma$ (no. 62)	−2.45	−2.33
P$_2$S$_5$	$P\bar{1}$ (no. 2)	−1.93	
SO$_3$	$Pna2_1$ (no. 33)	−4.84	−4.71

are the most stable. For the lithium phosphates, β-Li$_3$PO$_4$ has a lower energy than γ-Li$_3$PO$_4$ by 0.03 eV/formula unit; while for the lithium thiophosphates, γ-Li$_3$PS$_4$ has a lower energy than the most stable β-Li$_3$PS$_4$ structure by 0.09 eV/formula unit. Of the idealized β-Li$_3$PS$_4$ structures considered in this study, the β-Li$_3$PS$_4$-b was found to have the lowest energy with a lower energy than the β-Li$_3$PS$_4$-c structure by 0.03 eV/formula unit. The calculations also suggest that the β-Li$_3$PS$_4$-c' structure is difficult to physically realize because its computed energy is 0.1 eV/formula unit higher than that of the β-Li$_3$PS$_4$-b structure.

In addition to the main materials of the current study, the additional heat of formation results for related materials are also reported in Table III, including a few results repeated from the earlier work which were obtained using different PAW datasets.[16] Slight differences from the earlier numbers are indicative of the numerical accuracy of the method. Where possible, experimental values from Refs. 34 and 35 are listed.[36] The comparison with experiment is necessarily qualitative since finite-temperature effects were not taken into account in the calculations and the experimental data are often lacking precise phase information.

B. Li vacancies and interstitials

1. $Pmn2_1$ structured materials

Starting with the 128 atom supercell, we investigated the energies associated with creating a Li$^+$ vacancy or a Li$^+$ interstitial. The relative energy for forming a vacancy in the b site relative to that of the a site is 0.16 eV for β-Li$_3$PO$_4$, consistent with previous work,[7] while it is much smaller (−0.04 eV) for γ-Li$_3$PS$_4$.

Table IV lists the metastable interstitial sites found in β-Li$_3$PO$_4$ and γ-Li$_3$PS$_4$, showing interesting similarities. The results for β-Li$_3$PO$_4$ are nearly identical to our previous work.[7] For γ-Li$_3$PS$_4$, the geometries of the interstitial configurations are very similar to those of β-Li$_3$PO$_4$, but the relative energies are quite different. For example, the second lowest energy site for β-Li$_3$PO$_4$ is I_1. However in γ-Li$_3$PS$_4$, the I and II

TABLE IV. Li ion interstitial energies for Li_3PO_4 and Li_3PS_4 in the $Pnm2_1$ structure. The "I" site energy is set to 0.0 eV. A representative position of the site is given in terms of a representative fractional coordinate (x, y, z) referenced to the primitive unit cell.

Label	β-Li_3PO_4		γ-Li_3PS_4	
	Position	E (eV)	Position	E (eV)
I	(0.00, 0.45, 0.66)	0.00	(0.00 0.48 0.64)	0.00
I_1	(0.00, 0.42, 0.24)	0.30	(0.00 0.45 0.17)	0.44
II	(0.18, 0.00, 0.64)	0.37	(0.24 0.00 0.66)	0.00

sites have comparable energies, while the I_1 site has an energy similar to several other metastable interstitial sites that are much higher in energy than the I and II sites. The location of the distinct interstitial sites and their symmetric equivalents are visualized in Fig. 4 together with labeled vacancy sites.

We considered various Li$^+$ migration mechanisms for γ-Li_3PS_4 following a similar study for β-Li_3PO_4 presented in earlier work.[7] These are shown in Fig. 5 for diffusion paths along the **a** and **c** axes where the maximum migration barrier is found to be $E_m = 0.3$ eV. The paths from the NEB calculations are visualized in Fig. 5. Our analysis shows that the diffusion along the **b** axis is energetically less favorable. While we did not find any energetically favorable paths involving only the interstitial sites, the **a**-axis path between vacancy sites b_2 and a_2 passes close to the interstitial site of type II where it lowers the configuration energy.

The activation energy E_A for Li ion conduction within the electrolyte involves not only the migration energy E_m, but also the formation energy E_f. The formation energy involves the process of a Li ion moving from its perfect lattice site to form a vacancy and interstitial pair. Using reasonable assumptions of thermal equilibrium, the total activation energy E_A for ionic conductivity is given by[37]

$$E_A = E_m + \frac{1}{2}E_f. \qquad (4)$$

From our supercell model, we can estimate E_f for γ-Li_3PS_4. The lowest energy vacancy-interstitial defect structure that
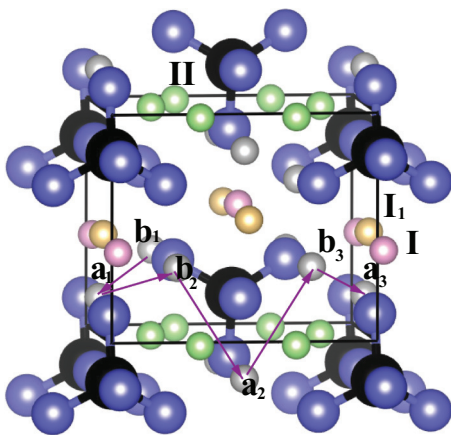

FIG. 4. (Color online) Ball and stick diagram of β-Li_3PO_4 with superposed interstitial sites. The Li, P, and O sites are depicted with gray, black, and blue balls respectively. The equivalent positions for the I, II, and I_1 sites are depicted with pink, green, and orange balls respectively.
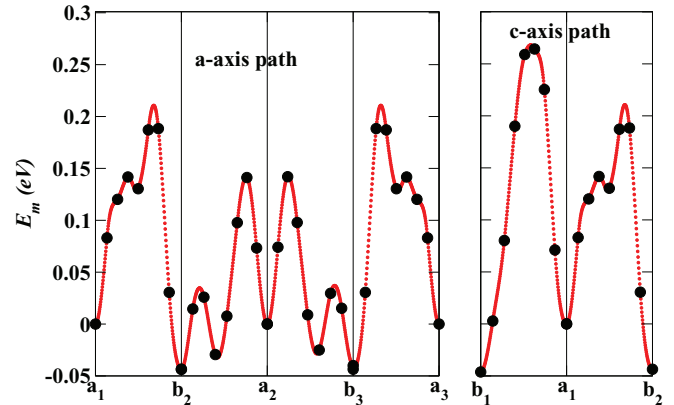

FIG. 5. (Color online) Energy diagram for Li vacancy migration along the **a** and **c** axes for γ-Li_3PS_4. The energy scale is taken to be the same as that given in Table IV; that is, zero energy is referenced to the configuration for the Li vacancy at a site of type a.

we have found so far is formed from a b vacancy and an interstitial of type II, with an energy $E_f = 0.8$ eV. From this analysis, our calculations estimate the activation energy for Li ion migration in γ-Li_3PS_4 to be $E_A = 0.7$ eV, which is larger than the experimental value[38] of $E_A = 0.5$ eV.[2,3] By contrast, previous calculations[7] estimated the activation energy for Li ion migration in β-Li_3PO_4, to be $E_A = 1.4$–1.6 eV with $E_f \approx 2.1$ eV.

2. Pnma structured materials

Starting with the 128-atom supercell, we investigated the energies associated with creating a Li$^+$ vacancy or a Li$^+$ interstitial. The main focus of this study is the β-Li_3PS_4-b material, since it is the closest to the experimentally observed structure. Although the detailed structures are different, the results for this lithium thiophosphate can be compared with those of γ-Li_3PO_4 studied in previous work.[7]

For γ-Li_3PO_4, the relative energy for forming a vacancy in the c site relative to that of the d site was found to be -0.21 eV.[7] By contrast, for β-Li_3PS_4-b, the relative energy for forming a vacancy in the b site relative to that of the d site was found to be 0.24 eV. The metastable interstitial site geometries were also found to be quite different for β-Li_3PS_4-b compared with γ-Li_3PO_4. For β-Li_3PS_4-b, the most stable interstitial site occurs at four sites equivalent to the site with fractional coordinates (0.94, 0.25, 0.72). This interstitial site can be characterized by the Wyckoff "c" label and its location is geometrically close to the c sites occupied in the β-Li_3PS_4-c and β-Li_3PS_4-c' structures listed in Table II. The structure of the ideal β-Li_3PS_4-b crystal with the most stable interstitial sites and site labels for possible migration paths is given in Fig. 6. Other metastable interstitial sites were found at relative energies 0.4 eV higher, located in the void channels of the crystal similar, but not identical to those found in γ-Li_3PO_4.[7]

Using the NEB analysis, we found plausible paths along each of the crystallographic directions as shown in Figs. 7 and 8. For the **a**-axis path shown in Fig. 7, which involves both b and d vacancy sites, the migration energy of $E_m = 0.3$ eV is controlled by the $b_1 \leftrightarrow d_1$ step. For the **b**-axis path shown in Fig. 8, which involves migration between d sites only, the
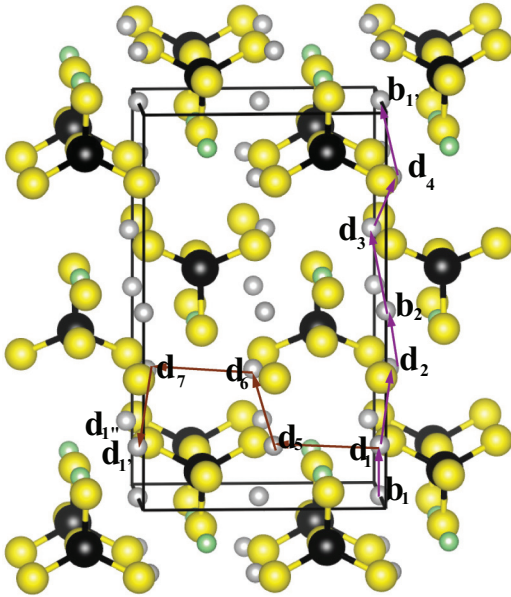
FIG. 6. (Color online) Ball and stick diagram of β-Li$_3$PS$_4$-b structure using the same convention used in Fig. 3 except the Li sites of the perfect lattice are indicated with gray balls, while the low-energy interstitial sites (having "c" symmetry) are indicated with green balls. The site labels are used to indicate possible vacancy migration paths.

migration energy is also found to be approximately $E_m = 0.3$ eV. This is caused by the fact that the vacancy migration step $d_1 \leftrightarrow d_5$ includes a lower energy configuration when the migrating ion passes the vicinity of the interstitial c site. The energy difference between this more stable configuration and the energy barrier during the $d_5 \leftrightarrow d_6$ step causes the overall migration energy to be $E_m = 0.3$ eV. In addition to the path shown in Fig. 8, another migration path along the **b** axis was found to have a migration barrier of $E_m = 0.2$ eV. This lower barrier path involves hopping between nearest-neighbor b vacancy sites. The most probable vacancy migration along the **c** axis was found to be a zigzag path between nearest-neighbor d sites which results in a migration barrier of $E_m = 0.2$ eV as shown in Fig. 8.
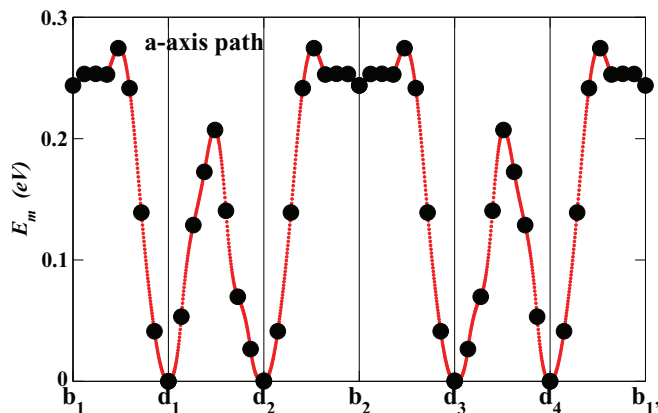

FIG. 7. (Color online) Energy diagram of NEB path for Li vacancy migration along the **a** axis for β-Li$_3$PS$_4$-b. The energy scale is zeroed at the configuration for the Li vacancy at the d site.
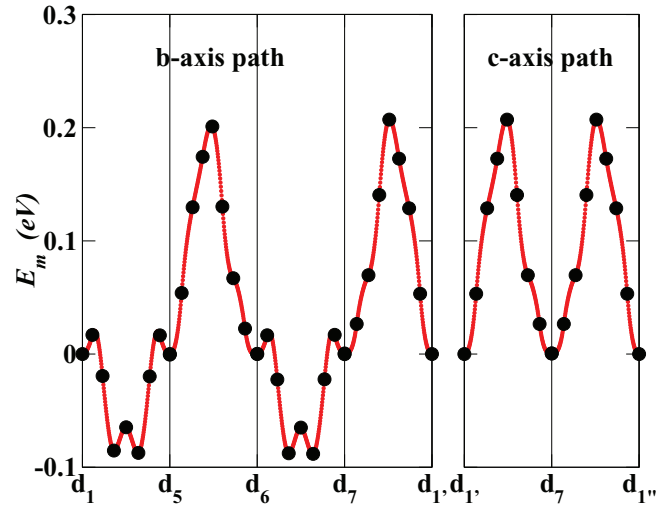

FIG. 8. (Color online) Energy diagram of NEB path for Li vacancy migration along the **b** and **c** axes for β-Li$_3$PS$_4$-b.

From our supercell model, we can estimate E_f for β-Li$_3$PS$_4$-b. For a vacancy-interstitial defect formed from a b vacancy and a c interstitial, we find $E_f = 0.1$ eV; for a vacancy-interstitial defect formed for a d vacancy and a c interstitial, we find $E_f = 0$ eV. These very small values of E_f indicate that there is a nearly temperature-independent population of vacancies/interstitials in this system and that the temperature-dependent conductivity is dominated by the migration energies; the calculated range of values of E_A for this system is between 0.2 and 0.3 eV. Experimental results are reported[1–3] in the range 0.4–0.5 eV. By contrast for γ-Li$_3$PO$_4$, the vacancy-interstitial pair was estimated to be 1.7 eV and E_A was estimated[7] to be in the range 1.1–1.3 eV in good agreement with experimental measurements.[39]

C. Interfaces

1. Interfaces of electrolyte with vacuum

In order to develop our understanding of electrolyte interfaces, we start with well-defined ideal surfaces in the presence of vacuum. The surface energy of a material measures the energy to cleave a surface of a bulk material. This can be related to the heat of formation according to the following formula normalized per formula unit:[40]

$$\Delta H_{\text{total}} = \Delta H_{\text{bulk}} + \sigma A. \tag{5}$$

Here ΔH_{total} represents the heat of formation per formula unit of the system in the slab geometry, ΔH_{bulk} represents the heat of formation of the bulk system per formula unit (as given in Table III for example), A represents the area of the slab per formula unit, and σ represents the extra energy per surface area associated with the surface formation.

Surface energies calculated for several surface planes of the Li$_3$PO$_4$ and Li$_3$PS$_4$ electrolytes are given in Table V. These were obtained for each configuration by fitting Eq. (5) from values of ΔH_{total} calculated for slabs of different thicknesses. In this study we focused on the surface configurations likely to represent the lowest energy structures. These were generated by assuming that no P-O or P-S bonds should be broken

TABLE V. Surface energies σ in units of eV/Å^2 for selected surface cleavage planes of Li$_3$PO$_4$ and Li$_3$PS$_4$.

Material	Plane	σ (eV/Å^2)
β-Li$_3$PO$_4$ ($Pmn2_1$)	[010]	0.039
γ-Li$_3$PO$_4$ ($Pnma$)	[100]	0.040
γ-Li$_3$PO$_4$ ($Pnma$)	[010]	0.073
γ-Li$_3$PO$_4$ ($Pnma$)	[100]^a	0.078
γ-Li$_3$PS$_4$ ($Pmn2_1$)	[010]	0.020
β-Li$_3$PS$_4$-b ($Pnma$)	[100]	0.020
β-Li$_3$PS$_4$-c ($Pnma$)	[100]	0.015
β-Li$_3$PS$_4$-c' ($Pnma$)	[100]	0.012

^{a}This represents a "rough" [100] surface due to an additional Li$_3$PO$_4$ group.

and that the system should remain neutral. The $Pmn2_1$ [010] cleavage is geometrically similar to the $Pnma$ [100] cleavage and the values of σ listed in Table V for both Li$_3$PO$_4$ and Li$_3$PS$_4$ show that these surfaces are the energetically most favorable. Table V lists results for a few other surfaces including a "rough" surface which have larger surface energies.

The total energy and stability of ideal thin films follows Eq. (5), which in most cases is governed by the bulk energy ΔH_{bulk}. Since the surface energy of the two most energetically favorable cleavages of Li$_3$PO$_4$ ([010] for β-Li$_3$PO$_4$ and [100] for γ-Li$_3$PO$_4$) are nearly identical we can conclude that the β-Li$_3$PO$_4$ structure is more stable than the γ-Li$_3$PO$_4$, even for very thin (large area/formula unit) films. However for Li$_3$PS$_4$, this is not the case.

Figure 9 plots ΔH_{total} versus surface area for several of the Li$_3$PS$_4$ slab simulations performed in this study. The integers in parentheses indicated on the plot report the number of unit-cell layers in each of the simulations slabs. The values at $A = 0$ were taken from the bulk results reported in Table III. Since the unit cell for γ-Li$_3$PS$_4$ contains only one layer of Li$_3$PS$_4$ along the **b** axis, thinner [010] slabs could be simulated compared with the β-Li$_3$PS$_4$ structures which contain two layers of

Li$_3$PS$_4$ along the **a** axis which are needed to construct [100] slabs. It is interesting that with the minor exception of the β-Li$_3$PS$_4$-c' structure, all of the results are accurately represented by a straight-line fit to Eq. (5), the slope of which determines the surface energy σ reported in Table V. Figure 9 also shows that for very thin layers of these ideal slabs (containing 1 unit cell in the layer), the β-Li$_3$PS$_4$-c and β-Li$_3$PS$_4$-c' structures have lower energy than the corresponding thin layers of the β-Li$_3$PS$_4$-b and γ-Li$_3$PS$_4$ structures.

2. Li$_3$PO$_4$ interface with Li

We investigated several ideal models of Li$_3$PO$_4$ surfaces in close proximity to metallic Li surfaces. An example simulation is shown in Fig. 10 which shows the relaxed structure of a two-layer [010] slab of β-Li$_3$PO$_4$ together with several layers of pure Li. By performing the calculations with several different initial Li slab geometries, we find that the qualitative results are insensitive to the number and structure of Li atoms in the slab representing the anode. Typically the relaxed structure accommodates the metallic Li atoms with an approximate volume of 18 Å^3 per atom.

Figure 10 shows a physically well-defined interface between the electrolyte and Li anode material. In addition to the physical stability of the interface, the partial density of states analysis suggests that the interface is chemically stable as well. Figure 11 shows the partial density of states of the supercell shown in Fig. 10. Here it is seen that the metallic states are energetically above the occupied electrolyte states. In this supercell the metallic states are separated from the electrolyte states with a small energy gap of 0.3 eV. This property is common to all of the lithium metal interfaces with lithium phosphate surfaces that we have studied. The Fermi level indicated in Fig. 11 depends on the number of metallic Li's included in the supercell (in this case 14). While LDA calculations such as those presented here typically underestimate band gaps of insulating materials, it is expected
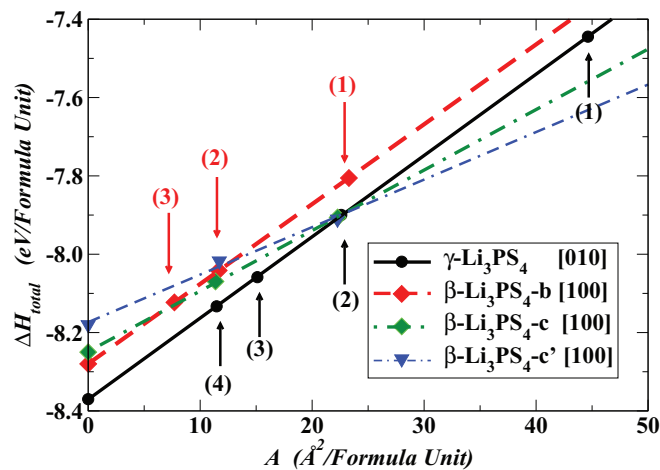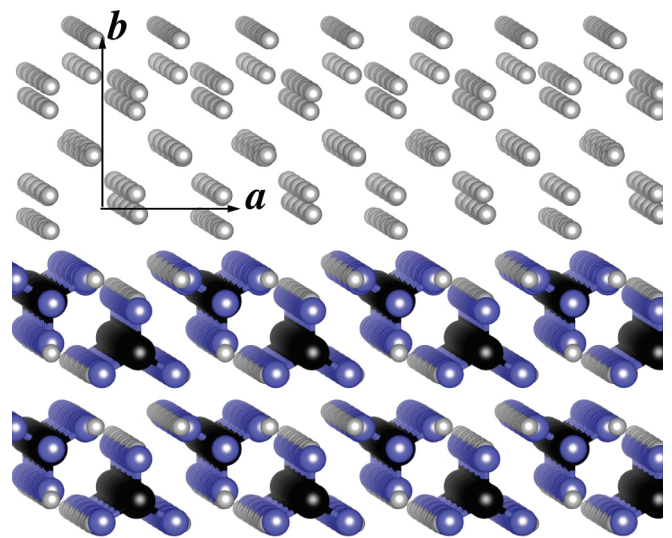

FIG. 9. (Color online) Plot of ΔH_{total} versus surface area A for slab calculations of various structures of Li$_3$PS$_4$ with various slab thicknesses. The lines correspond to Eq. (5). The integers in parentheses indicate the number of unit cell layers in each of the simulation slabs.

FIG. 10. (Color online) Ball and stick representation of optimized structure of an ideal [010] slab of β-Li$_3$PO$_4$ with several layers of Li. The supercell contains four formula units of β-Li$_3$PO$_4$ and 14 Li atoms. The Li, P, and O sites are depicted with gray, black, and blue balls, respectively.
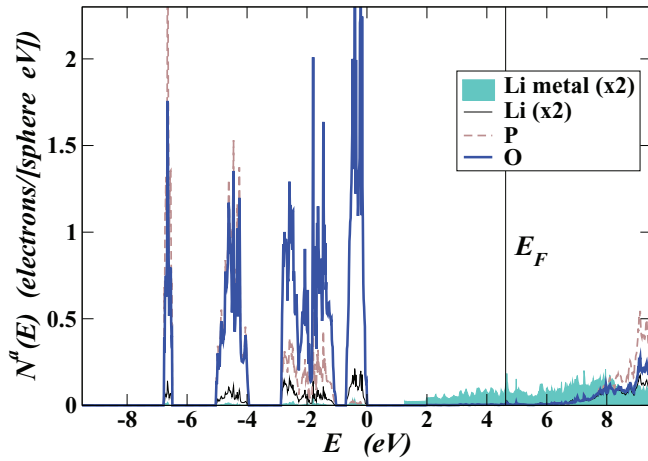
FIG. 11. (Color online) Partial density of states plot of β-Li$_3$PO$_4$ electrolyte in the Li presence of Li layers as shown in Fig. 10. The energy scale for the plot was adjusted to the top of the filled valence band of the β-Li$_3$PO$_4$ layer. The weight factors for the partial densities of states are given by Eq. (2) for each type of atomic site a, averaged over sites of the same type.

that the qualitative features of the partial densities of states are reliable.

3. Li$_3$PS$_4$ interface with Li

In contrast with the lithium phosphate materials, models of ideal Li$_3$PS$_4$ surfaces were found to be structurally (and chemically) altered by the presence of Li metal atoms as shown in Fig. 12. In this example, a two-layer [010] slab of γ-Li$_3$PS$_4$ is prepared in vacuum and one Li atom per formula unit is placed in the vacuum region of the supercell [Fig. 12(a)]. After this initial configuration is allowed to relax, the thiophosphate ions at the surface layer are found to be significantly altered in the relaxed structure, as shown in Fig. 12(b). The (meta)stable structure shown in Fig. 12(b) was generated by the optimization algorithm of the QUANTUM ESPRESSO software[18] and may not represent a physically realizable structure. On the other hand, the qualitative result that metallic Li breaks the S-P bonds at a surface of γ-Li$_3$PS$_4$ is a clear conclusion of this analysis. We observed similar behavior for several different initial Li slab geometries and for simulations of slabs of β-Li$_3$PS$_4$ in the presence of Li metal as well.
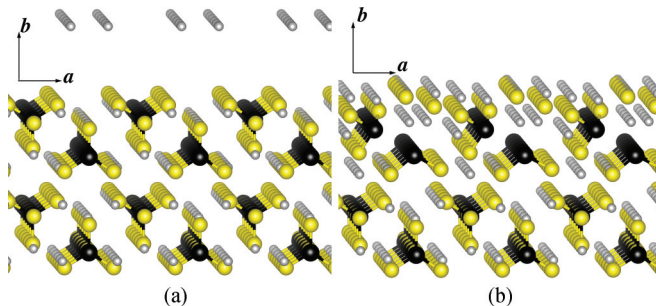

FIG. 12. (Color online) Ball and stick representation of Li$_3$PS$_4$ surfaces with Li, P, and S sites depicted with gray, black, and yellow balls, respectively. (a) Ideal [010] slab of γ-Li$_3$PS$_4$ with initial position of Li atoms. The supercell contains four formula units of γ-Li$_3$PS$_4$ and four Li atoms. (b) Relaxed structure of configuration (a).
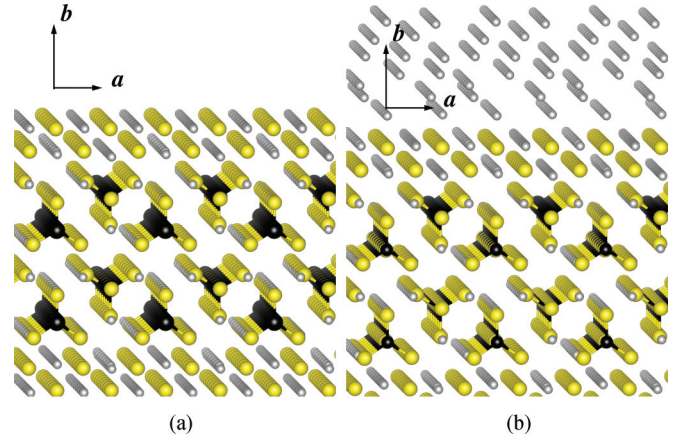

FIG. 13. (Color online) (a) Relaxed structure of a [010] slab of γ-Li$_3$PS$_4$ with buffer layers of Li$_2$S. The supercell contains four units of Li$_3$PS$_4$ and eight units of Li$_2$S. (b) Relaxed structure of buffered electrolyte shown in (a) with the addition of 14 Li atoms in the supercell.

While these computational results clearly indicate that metallic Li reacts with the Li$_3$PS$_4$ electrolyte, the experimental literature suggests otherwise. For example, it has been shown[1] that Li$_3$PS$_4$ can be cycled many times with a Li metal anode. One possible explanation of the apparent stability of the Li$_3$PS$_4$ electrolyte is that a stable thin buffer layer containing Li$_2$S is formed during the first few cycles.[41] In order to explore
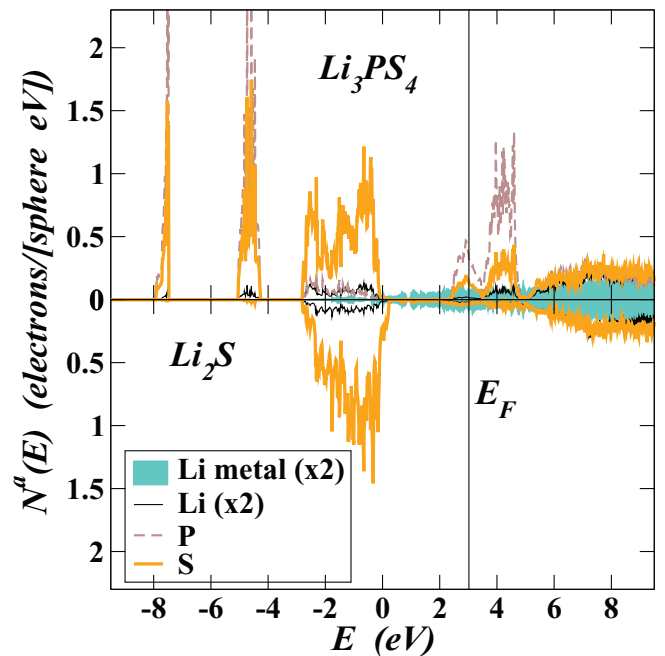

FIG. 14. (Color online) Partial density of states plot of γ-Li$_3$PS$_4$ electrolyte, buffered with Li$_2$S in the presence of Li layers as shown in Fig. 13(b). The upper panel shows the states associated with the γ-Li$_3$PS$_4$ and the lower panel shows the states associated with the Li$_2$S buffer layer. Both panels show the contributions from the metallic Li layer. The energy scale for the plot was adjusted to the top of the filled valence band of the γ-Li$_3$PS$_4$ layer. The weight factors for the partial densities of states are given by Eq. (2) for each type of atomic site a, averaged over sites of the same type.

this possibility computationally, we added a two-layer "thin film" of Li_2S on both sides of the γ-Li_3PS_4 slab as shown in Fig. 13(a). The thin film of cubic Li_2S was oriented in its nonpolar [110] direction. The optimized lattice constants for the composite slab are within 0.1 Å of those computed for vacuum conditions. Two Li_2S groups are accommodated along the **a** axis with a compression of approximately 0.3 Å, while one Li_2S group is accommodated along the **c** axis with an expansion of approximately 0.4 Å in comparison to cubic Li_2S. While the construction of this buffer layer is not unique, this structure was found to be very stable with a binding energy of -0.9 eV/(reference unit) compared with the separated units calculated in the same supercell. (In this case the reference unit is Li_3PS_4 plus $2Li_2S$.) Now, when Li metal is introduced in the vicinity of the buffered Li_3PS_4 electrolyte slab, a stable interface between the electrolyte and Li metal is achieved as shown in Fig. 13(b).

Investigating the buffered electrolyte system [Fig. 13(b)] further, we determined the partial density of states of the system as shown in Fig. 14. Here we see that, while the energy distribution of the electrolyte and anode states are not as well separated as in the lithium phosphate case, most of the metallic spectrum lies energetically above the electrolyte and buffer states.

IV. SUMMARY AND CONCLUSIONS

The literature reporting experimental studies of lithium (thio)phosphates has generated a number of basic materials questions:

(1) What is the cause of the differences between the bulk phases of Li_3PO_4 and Li_3PS_4; particularly what causes the fractional occupancies of the Li site configurations found in β-Li_3PS_4?

(2) What is the mechanism for stabilizing the high-temperature phase β-sulfur structure at room temperature and the corresponding improvement in ionic conductivity described in Ref. 1?

(3) How is it possible to stabilize the interface between pure Li_3PS_4 and metallic lithium?

The results of the present simulations can be used to partially answer these questions.

On the subject of the bulk crystal structures, we can say the following. The simulations do a very good job of modeling the competing interactions which determine the most energetically favorable crystalline geometries. In particular, the observation that both Li_3PO_4 and Li_3PS_4 have their lowest energy structures with $Pmn2_1$ symmetry is well represented by the simulations. For the higher energy structures with $Pnma$ symmetry, the detailed structures are more complicated. The simulations show that the most stable Li_3PO_4 structure with $Pnma$ symmetry (γ-Li_3PO_4) corresponds to a Li_3PS_4 structure which we call β-Li_3PS_4-c' which has relatively high energy and is therefore unlikely to be physically realizable. The simulations find the most stable ordered configuration of β-Li_3PS_4 (which we call β-Li_3PS_4-b) is characterized by 100% occupation of the b and d sites. As shown in Table II, this ideal structure compares well with the experimental structure which has 70% occupation of the b sites, 30% occupation of the c sites, and 100% occupation of the d sites. While our

simulations cannot directly account for the fractional site occupancies, the supercell simulations of the β-Li_3PS_4-b structure show that the most energetically favorable interstitial site of the material has c symmetry and has fractional coordinates close to those of the simulated β-Li_3PS_4-c and β-Li_3PS_4-c' structures and to those of the related experimental analysis. It is also interesting that the simulations show that the formation energy for a vacancy-interstitial pair in the β-Li_3PS_4-b structure is $E_f \leqslant 0.1$ eV. Therefore, it seems likely that a Boltzmann populations argument could be made in support of the partial occupancy of the Li sites in the β-Li_3PS_4 structure that has been reported in the experimental literature.[2–4]

In addressing the stabilization mechanism for β-Li_3PS_4 in the nanoporous structure described in Ref. 1, we initially investigated the structural stability of very thin ideal slabs. From the results presented in plots of total energy versus surface area shown in Fig. 9, surface energies can effect the lowest energy phase for very thin ideal films. However, this effect is likely to be of academic (not practical) interest, since it occurs only for extremely thin films under ideal vacuum conditions. On the other hand, there are many examples in the literature of metastable structures being formed with the help of kinetic barriers which inhibit phase transitions to lower energy states. This may be an appropriate explanation for existence of the β-Li_3PS_4 structure at room temperature.

The calculated results for the ion migration energies in idealized models of Li_3PS_4 are not in numerical agreement with the published experimental results. The experimental measurements[1–3] indicate that $E_A = 0.5$ and 0.4 eV for the γ and β structures respectively. Our simulation results for the γ phase overestimate experiment with $E_A = 0.7$ eV, while for the β phase, they underestimate experiment with $E_A = 0.2$ or 0.3 eV. For both phases, the NEB simulations estimate the ion migration energies to be $E_m = 0.2$–0.3 eV. However, our estimates of the "formation" energy E_f for an interstitial-vacancy pair are very different for the two Li_3PS_4 structures. For γ-Li_3PS_4, the most energetically favorable energy that we have found so far is $E_f = 0.8$ eV. On the basis of Eq. (4), the calculated activation energy is $E_A = 0.7$ eV. Perhaps a smaller E_f can be found for this material that would put the simulations closer to the experimental finding. For the β phase, the most energetically favorable formation energy is essentially negligible, and $E_A \approx E_m$. It is reasonable to speculate that this underestimate of E_A for β-Li_3PS_4 is due to the neglect of additional contributions to the activation process at the electrolyte boundaries due to buffer layers which exist on the outer surfaces. Additional simulations are needed to investigate this possibility.

On the subject of the interface structures between the electrolyte and lithium metal, our results are very interesting. The simulations of an interface between Li_3PO_4 and metallic lithium indicate ideal behavior with physical and chemical stability as illustrated in Figs. 10 and 11. Another measure of phase stability developed by Ong *et al.*[42] comes from the consideration of the possible decomposition of the electrolyte in the presence of a reservoir of metallic Li.[43] From the heat of formation results presented in Table III, the reaction

$$Li_3PO_4 + 8Li \rightarrow Li_3P + 4Li_2O \qquad (6)$$
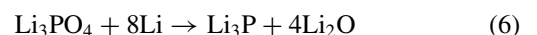
is predicted to be exothermic, suggesting that the Li_3PO_4/Li interface is thermodynamically unstable. However, the results presented in Sec. III C2 suggest that there is a significant kinetic barrier in this system which stabilizes the interface in the absence of any external fields. Presumably this barrier is related to the energetic and physical confinement of the metallic electron density within the anode slab making them unavailable to participate in the decomposition reaction of Eq. (6). In fact, the reaction described by Eq. (6) requires the addition of eight electrons to transform the form of phosphorus from P^{+5} in Li_3PO_4 to P^{-3} in Li_3P. While our ideal simulations do not consider the effects of an external electric field and other aspects of real battery operation, the computed stability of the Li_3PO_4 interface is consistent with the experimental studies of the related LiPON/Li interface which has been shown to maintain its basic structure even after thousands of Li cycles.[44]

By contrast, the results of our simulations illustrated in Figs. 12 and 13 show that even for an idealized structure of Li_3PS_4, the stability issue is nontrivial. We have shown that the pure Li_3PS_4 surface is unstable in the presence of Li metal, but that a very thin buffer layer of Li_2S can protect the surface from degradation. In the experimental processing, it is possible that this buffer layer forms naturally during the first few cycles of battery operation, much like the solid-electrolyte interphase (SEI) layer forms in liquid electrolytes. Not surprisingly, from the heat of formation results presented in Table III, the reaction

$$Li_3PS_4 + 8Li \rightarrow Li_3P + 4Li_2S \qquad (7)$$
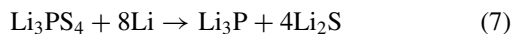
is predicted to be highly exothermic, suggesting that the Li_3PS_4/Li interface is thermodynamically unstable. Presumably, the buffer layer can provide a kinetic barrier by confining the electron density to the anode region and inhibiting the electron availability needed to change the charge state of phosphorus as discussed for the Li_3PO_4 case above. It is reasonable to speculate that the increased ionic conductivity reported[1] for nanoporous β-Li_3PS_4 (compared with other preparations of β-Li_3PS_4) might be due to the stabilization of a favorable SEI compared to that of other preparations. Further modeling work is needed to study how the buffer layer effects the overall conductivity and performance of the electrolyte. Further collaboration between modeling and experiment could compare the properties of an ideal buffer layer such as that modeled in the present work with the properties of a buffer layer formed in experimental conditions by cycling a pure Li_3PS_4/Li cell.

*Corresponding author: natalie@wfu.edu

†Present address: Institute of Atomic and Molecular Sciences, Academia Sinica, Taipei, 10617, Taiwan.

[1] Z. Liu, W. Fu, E. A. Payzant, X. Yu, Z. Wu, N. J. Dudney, J. Kiggans, K. Hong, A. J. Rondinone, and C. Liang, J. Am. Chem. Soc. **135**, 975 (2013).

[2] K. Homma, M. Yonemura, T. Kobayashi, M. Nago, M. Hirayama, and R. Kanno, Solid State Ionics **182**, 53 (2011).

[3] M. Tachez, J.-P. Malugani, R. Mercier, and G. Robert, Solid State Ionics **14**, 181 (1984).

[4] R. Mercier, J.-P. Malugani, B. Fahys, G. Robert, and J. Douglade, Acta Crystallogr. **B38**, 1887 (1982).

[5] A. K. Ivanov-Shitz, V. V. Kireev, O. K. Mel'nikov, and L. N. Demainets, Crystallogr. Rep. **46**, 864 (2001).

[6] C. Keffer, A. Mighell, F. Mauer, H. Swanson, and S. Block, Inorg. Chem. **6**, 119 (1967).

[7] Y. A. Du and N. A. W. Holzwarth, Phys. Rev. B **76**, 174302 (2007).

[8] Y. A. Du and N. A. W. Holzwarth, J. Electrochem. Soc. **154**, A999 (2007).

[9] K. Takada, Acta Mater. **61**, 759 (2013).

[10] M. Tatsumisago and A. Hayashi, Solid State Ionics **225**, 342 (2012).

[11] A. Hayashi and M. Tatsumisago, Electron. Mater. Lett. **8**, 199 (2012).

[12] N. Kamaya, K. Homma, Y. Yamakawa, M. Hirayama, R. Kanno, M. Yonemura, T. Kamiyama, Y. Kato, S. Hama, K. Kawamoto, and A. Mitsui, Nat. Mater. **10**, 682 (2011).

[13] P. Hohenberg and W. Kohn, Phys. Rev. **136**, B864 (1964).

[14] W. Kohn and L. J. Sham, Phys. Rev. **140**, A1133 (1965).

[15] P. E. Blöchl, Phys. Rev. B **50**, 17953 (1994).

[16] N. A. W. Holzwarth, A. R. Tackett, and G. E. Matthews, Comput. Phys. Commun. **135**, 329 (2001).

[17] X. Gonze et al., Comput. Phys. Commun. **180**, 2582 (2009); code is available at the website http://www.abinit.org.

[18] P. Giannozzi et al., J. Phys.: Condens. Matter **21**, 394402 (2009); available from the website http://www.quantum-espresso.org.

[19] J. P. Perdew and Y. Wang, Phys. Rev. B **45**, 13244 (1992).

[20] J. P. Perdew, K. Burke, and M. Ernzerhof, Phys. Rev. Lett. **77**, 3865 (1996); **78**, 1396(E) (1997).

[21] H. Jónsson, G. Mills, and K. W. Jacobsen, in Classical and Quantum Dynamics in Condensed Phase Simulations, edited by B. J. Berne, G. Ciccotti, and D. F. Coker (World Scientific, Singapore, 1998), pp. 385–404.

[22] G. Henkelman, B. P. Uberuaga, and H. Jónsson, J. Chem. Phys. **113**, 9901 (2000).

[23] G. Henkelman and H. Jónsson, J. Chem. Phys. **113**, 9978 (2000).

[24] Similar capabilities are currently being implemented into the QUANTUM ESPRESSO (Ref. 18) package.

[25] N. A. W. Holzwarth, G. E. Matthews, R. B. Dunning, A. R. Tackett, and Y. Zeng, Phys. Rev. B **55**, 2005 (1997).

[26] A. Kokalj, J. Mol. Graphics Modell. **17**, 176 (1999); code available at the website http://www.xcrysden.org.

[27] A. Kokalj, Comput. Mater. Sci. **28**, 155 (2003).

[28] K. Momma and F. Izumi, Appl. Crystallogr. **44**, 1272 (2011); code available from the website http://jp-minerals.org/vesta/en/.

[29] *International Tables for Crystallography, Volume A: Space-group Symmetry*, Fifth revised edition, edited by T. Hahn (Kluwer, Dordrecht, 2002).

[30] To the best of our knowledge this nomenclature for Li$_3$PS$_4$ was set in Ref. 2. An earlier publication of our group (Ref. 31) used a different nomenclature.

[31] N. A. W. Holzwarth, N. D. Lepley, and Y. A. Du, J. Power Sources **196**, 6870 (2011).

[32] O. V. Yakubovich and V. S. Urusov, Crystallogr. Rep. **42**, 261 (1997).

[33] Y. A. Du and N. A. W. Holzwarth, Phys. Rev. B **81**, 184106 (2010).

[34] *CRC Handbook of Chemistry and Physics, 92th Edition*, edited by W. M. Haynes (CRC, Taylor & Francis Group, London, 2011).

[35] M. W. Chase, Jr., C. A. Davies, J. R. Downey Jr., D. J. Frurip, R. A. McDonald, and A. N. Syverud, "NIST JANAF Thermochemical Tables 1985", (1986); website: kinetic.nist.gov.

[36] The experimental values of materials containing O and N were used to set the standard energies of those elements which are both in the form of diatomic molecules.

[37] A. R. West, *Basic Solid State Chemistry*, 2nd ed. (John Wiley & Sons, New York, 1999).

[38] The results from Ref. 2 were assumed to need a correction of ln(10).

[39] B. N. Mavrin, V. V. Asonov, V. V. Fomichev, A. K. Ivanov-Shitz, and V. V. Kireev, J. Exp. Theor. Phys. **96**, 53 (2003).

[40] J. M. Howe, *Interfaces in Materials* (John Wiley & Sons, New York, 1997).

[41] C. Liang and N. Dudney (private communication).

[42] S. P. Ong, Y. Mo, W. D. Richards, L. Miara, H. S. Lee, and G. Ceder, Energy Environ. Sci. **6**, 148 (2013)

[43] We thank the referee for this argument.

[44] N. J. Dudney, Interface **17**(3), 44 (2008).